



## OPEN Influence of Cu and Co addition on metallurgical and wear characteristics of AlCrFeNi high entropy alloy

M. Vignesh<sup>1</sup>, M. Sujit<sup>1</sup>, N. Radhika<sup>2</sup>, M. Sathishkumar<sup>1✉</sup>, S. M. Muthu<sup>3</sup>, Khushbu Dash<sup>4</sup> & Soumya Ranjan Mishra<sup>5</sup>

The creation of new alloys with improved qualities has become essential in modern industries for high-performance materials. This work's main objective is to use vacuum arc melting (VAM) to synthesize two different high-entropy alloys (HEAs): AlCrFeNiCu and AlCrFeNiCo. The mechanical properties, phase composition, grain boundaries, and alloy composition of the HEAs were studied. The predominant crystal structure, the Body-Centred Cubic (BCC) phase was obtained for both alloys. Significantly, the Co-containing HEA showed a smaller particle size than the Cu-containing HEA, which led to a 14.21% increase in microhardness. It indicates that the Co-based HEA will likely perform better than the Cu-based HEA in applications prone to abrasion, and indentation, and requiring high hardness levels based on the observed microstructure and hardness parameters. According to wear surface morphology studies, main effects analysis and ANOVA show that increasing loads and sliding distances increase wear rate, whereas sliding velocity has less effect. The best wear rate-reducing parameters are 10 N, 0.5 m/s, and 500 m for Cu-containing HEAs, and the same can be predicted using regression analysis. The study categorizes the intricate worn surface structure by describing different surface properties and wear mechanisms, such as grooves, delamination, adhesive wear, and pitting.

**Keywords** Vacuum arc melting, High entropy alloy, X-ray techniques, Grain boundaries, Indentation and hardness, Electron backscatter diffraction

High Entropy Alloys (HEAs) have been studied extensively in materials science since they consist of multiple elements that are present in nearly equiatomic ratios. These alloys generally develop stable solid solutions that have a superior performance in mechanical, thermal, and chemical aspects compared to the customary alloys<sup>1,2</sup>. HEAs can be produced using various methods, namely advanced techniques of AM such as Selective Laser Melting (SLM) and Directed Energy Deposition (DED) and conventional techniques like Vacuum Arc Melting (VAM) and powder metallurgy. The method of synthesis is usually crucial in determining properties such as corrosion resistance, ductility, and strength, hence the flexibility of these alloys for miscellaneous uses. In particular, VAM has been widely employed in synthesising HEAs with desirable characteristics<sup>3</sup>. Out of these methods, VAM has been widely preferred because it can create HEAs with desired properties such as enhanced microstructure and hardness. For instance, Nahmany et al. have illustrated that Al<sub>x</sub>CrFeCoNi HEAs produced by VAM yielded better hardness when electron beam surface remelting was employed to even further increase the material properties through fine grains<sup>4</sup>. Further, other findings by Miracle and Senkov demonstrated that the refractory HEAs formed through VAM could attain high micro-hardness and the stable single-phase body-centred cubic (BCC) phase, which is useful for high-temperature and wear-resistant applications<sup>5</sup>.

For HEAs, the properties are highly dependent on the elements of the system and the processing technique applied. Some of the oxidation and corrosion-resistant elements include aluminum (Al), copper (Cu), and chromium (Cr) while the wear resistance and hardness are provided by iron (Fe) and nickel (Ni)<sup>6–8</sup>. The specific choice of the alloying elements has a direct impact on the overall performance, cost, and technological

<sup>1</sup>Department of Mechanical Engineering, Amrita School of Engineering, Amrita Vishwa Vidyapeetham, Chennai, India. <sup>2</sup>Department of Mechanical Engineering, Amrita School of Engineering, Amrita Vishwa Vidyapeetham, Coimbatore, India. <sup>3</sup>Department of Nuclear and Quantum Engineering, Korea Advanced Institute of Science and Technology, Daejeon 34141, Republic of Korea. <sup>4</sup>Department of Chemistry, Amrita School of Engineering, Amrita Vishwa Vidyapeetham, Chennai, India. <sup>5</sup>Department of Metallurgical and Materials Engineering, Indian Institute of Technology, Madras, Chennai 600036, India. ✉email: m\_sathishkumar@ch.amrita.edu

applicability of HEAs. Recent research has been directed to low-cost HEAs comprised of Fe, Mn, Cu, Ni, and Al, where an effort has been made to meet the performance criterion, excellent mechanical properties at high temperatures, and cost limitation<sup>9</sup>.

Most of the HEAs create different crystal structures, such as the face-centred cubic (FCC), body-centred cubic (BCC), and hexagonal close-packed (HCP) phase. The most typical lattices are the FCC and BCC structures; they have the same lattice parameters, and high ductility is characteristic of FCC, whereas BCC has greater yield strength, but it is more brittle<sup>10</sup>. According to the literature, it has been proven that oxidation can be reduced when there is a higher purity of aluminum in the AlxCrCuFeNi HEAs thus illustrating how the composition of HEAs influences their performance<sup>11</sup>. HEAs also demonstrated excellent wear resistance at high temperatures, depending on the microstructure, grain size, and precipitation.

Researching the wear behaviour of AlCoCrFeNi alloy system has shown improved wear resistance with the addition of aluminum in its composition which helps in refining the surface of the alloy and increasing its surface hardness. The wear rate of these alloys is therefore inversely proportional to hardness, especially at high loads<sup>12</sup>. Furthermore, the wear behavior is also influenced greatly by temperature, where oxidation wear is most likely to occur at 600 °C. This indicates that through the application of AlCoCrFeNi coatings, mechanical properties' improvement is achieved in addition to coating adhesion and anti-friction characteristics<sup>13</sup>. The leading cause of wear prone to the magnesium matrix was abrasive wear, while the AlCoCuFeNi particles conveyed the HEAs capability to resist fatigue wear and it is 45% higher<sup>14</sup>.

In this context, the present study focuses on two HEA systems: Two of the alloy compositions which are AlCrFeNiCu and AlCrFeNiCo were prepared by the VAM technique. These systems are selected according to their favourable mechanical and wear resistance characteristics. It is also important to note that Al, Cu, Ni, and Co help in the formation of a stable FCC phase and Cr and Fe in the formation of the BCC phase. AlCrFeNiCu has a great advantage in being plastic, oxidation resistant, and inexpensive because as there is no cobalt. However, its strength remains somewhat lower as compared to that of AlCrFeNiCo. This is superior in strength conditions, which are always preferred for high-load conditions. These trade-offs include less plasticity and higher brittleness for the AlCrFeNiCo alloy, since the phase is BCC.

This work differs from the prior research on similar HEAs in relation to their microstructure and wear behaviour, the present work takes a unique aspect by directly comparing the implications of Cu and Co addition at identical experimental conditions. This allows discriminating the distinctive perspective of the role of these elements on phase stability, grain refinement, hardness and the wear resistance of HEAs and thus provides the necessary information for compositional control and valuable insights for industrial applications. The goals and scope are to study the metallurgical properties, phase stability, and mechanical behaviour of these HEAs and to discover compositions which would be useful in service in harsh conditions.

## Materials and methods

This research specifically focuses on the evaluation of AlCrFeNiCo and AlCrFeNiCu based High Entropy Alloys (HEAs) produced by the Vacuum Arc Melting (VAM) method. This technique is heavily used for producing alloys in different quantities to obtain precise properties. The key elements such as nickel (Ni), chromium (Cr), aluminium (Al), iron (Fe), copper (Cu), and cobalt (Co), are very pure and are protected by the VAM chamber (High Vacuum Instruments Ltd.) in an argon atmosphere. Each of these elements has purity levels far above 99.9 wt%. The VAM was performed inside the electric arc furnace under high vacuum pressures normally falls within  $10^{-3}$  to  $10^{-6}$  torr. An electric arc necessary for this melting process of alloying elements was created using an electrode made from non-consumable tungsten. The melt resulting from such a melting procedure was collected in a water-cooled copper crucible and further the ingots. During this process of melting, the impurities in the alloy are removed effectively due to their selective vaporization, hence resulting in almost pure alloys. Pre-melting and re-melting of raw materials for the elements of choice 3 to 5 times guarantee uniform single-phase HEA. This cyclic melting process also provides a uniform mixing of elements and guarantees a typical microstructure. This current study expounds on the methods as illustrated in Fig. 1.

After the VAM process, the samples were grounded and subjected to a standard metallographic procedure including polishing with different SiC abrasive papers and alumina suspension to attain a mirror-like finish. This step is essential for the precise microstructural characterisation of prepared HEA samples. Phase structures are characterised using Bruker D8 X-ray diffractometer with Cu-K $\alpha$  source radiation. This device also affords the means of moving repeatedly through a 2 $\theta$  survey from 25° to 90° with a consistency of 0.2 °/min. Thus, through the help of EDX (e), it is possible to have a detailed analysis of the alloy and know the content of the elements that are in it. Employing Quanta 3D FEG, the EBSD examination for HEA demonstrates the grain size, phase composition, Schmid factor, and misorientation angle because of the extensive investigation of the as-cast material. The nominal and measured compositions of HEAs are mentioned in Table 1.

To find out the mechanical characteristics of the alloys, more work is carried out. There is the use of the Matsuzawa MMT-X device and the method of Vickers micro-hardness testing, which is done by following the guidelines of ASTM E384 standard. The averages of six trials are taken, where the load of 100 g was applied for 15 s for each trial. Wear tests are carried out on the prepared specimens with three varying levels of load, sliding speed and sliding distance using a Pin-on-disc tribometer. During the wear test, the D2 Tool steel disk was used as a counterpart. The testing process does not employ any lubrication, ensuring that the wear behaviour of the material is assessed under dry sliding conditions with an ambient temperature of 27 °C and relative humidity of 65%, which are commonly encountered in real-world applications. The purpose of these environmental settings is to accurately simulate real-life operational conditions and ensure that the experimental findings may be applied to real-world situations. A stress sensor is used to measure the specimen's frictional force. The frictional coefficient, an essential parameter that provides insight into the tribological characteristics of a material, must be determined through the measurement of the frictional force. Through precise real-time monitoring of the



**Fig. 1.** Significant steps involved in current research.

AlCrFeNiCu			AlCrFeNiCo		
Element	Nominal composition (at%)	Measured composition (at%)	Element	Nominal composition (at%)	Measured composition (at%)
Al	20	18.7	Al	20	19.2
Cr	20	19.8	Cr	20	19.5
Ni	20	19.4	Ni	20	20.3
Fe	20	20.7	Fe	20	21.2
Cu	20	21.4	Co	20	19.8

**Table 1.** Nominal and measured composition of HEAs.

Factors	Levels		
Load (N)	10	25	40
Velocity (m/s)	0.5	2.0	3.5
Sliding Distance (m)	500	1250	2000

**Table 2.** Wear test parametric levels.

frictional force and frictional coefficient, the software of the tribometer can yield important information on how the material reacts to sliding wear in the given circumstances. Wear test parameters and their levels are given in Table 2.

It is concluded that the best combination of factors that makes the wear parameters optimum has been determined using the Mean Effects method, and the influence of various input parameters on wear has been analysed. Observations yielding rankings from the patterns of experimental data can be drawn. An orthogonal array has been used for the analysis with the data derived from nine experiments. So, a range of influence of process parameters on the wear behaviour of samples was done. The analysis of Variance (ANOVA) method was used as a statistical tool to examine and quantify the effect of various parameters on material properties leading to wear.

## Results and discussion

### Phase analysis

The XRD plots of as-cast HEA specimens are displayed in Fig. 2a<sub>1</sub> and a<sub>2</sub>. This technique is critical in making the material's atom-by-atom structure evident to understand its features and applications. From the XRD data, it can be concluded that the HEAs under investigation contain FCC as well as BCC forms. Of the HEAs with different elements, it can be seen that the structure of the HEAs with Copper (Cu) and Cobalt (Co) elements was identified by FCC and BCC peaks, respectively. The XRD analysis pattern for the AlCrFeNiCu high entropy alloy shows the existence of the FCC phase. It is evident from the obtained XRD peaks at (111), (200) and (220), the dominant FCC phase is confirmed. This is mainly due to the presence of Copper (Cu) and its interaction within the HEA alloy. The observed FCC peaks further confirm the structural homogeneity within the chosen alloy composition and its atomic arrangement favours the enhanced mechanical properties and stability of the alloy. Besides the minor diffraction peaks corresponding to the BCC structure are also seen from the XRD-spectrum results, as supported by other studies<sup>15</sup>.

The diffraction peaks belonging to the BCC phase are (200), (211), and (110) which are exhibited in both the fabricated HEAs and thus endorse the conclusion. This is indeed significant knowledge that offers discernible proof of the crystal structure that prevails in the materials being studied. With the value of negative mixing enthalpy, the observation of the BCC phase can be explained, which is estimated to be  $-22$  kJ/mol. The negative value of enthalpy helps in the proper miscibility of different elements within the framework of the alloy and gifts the BCC crystal structure with desirable characteristics like alloying<sup>16</sup>. This case illustrates the role that thermodynamical parameters play in the formation of the phases in the HEAs. Hence, the AlCrFeNiCu alloy has a comparatively higher microhardness than the AlCrFeNiCo alloy due to the BCC phase. Thus, the unique constitution of the newly developed AlCrFeNiCo alloy promotes the development of a body-centred cubic (BCC) phase with improved mechanical characteristics, hence the increased microhardness. Another change worth mentioning is the secondary phase absence in the developed HEAs. It is missing, as HEAs have inherently higher configurational entropy by their nature as alloying systems. APPER has defined configurational entropy as the amount of disorder associated with the atomic positioning in a solid solution. Thus, many elements in HEAs with equiatomic or nearly equiatomic compositions show a substantial configurational entropy increase. This results in the Gibbs free energy decrease and improves the overall stability of the phase that is synonymous

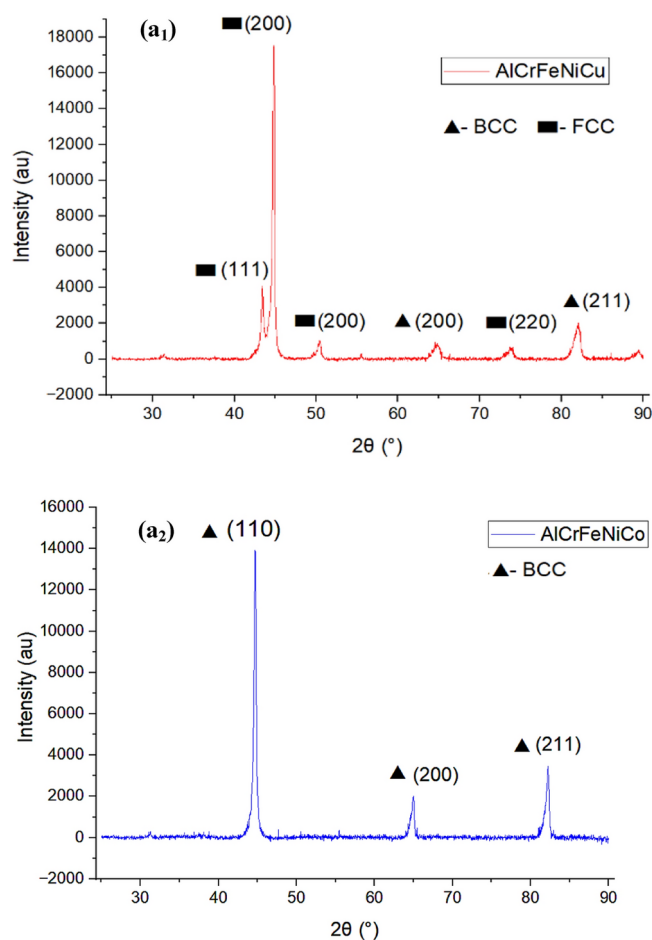


**Fig. 2.** XRD patterns of (a<sub>1</sub>) AlCrFeNiCu, (a<sub>2</sub>) AlCrFeNiCo HEAs.

with solid solutions. Hence, the sub-phase's absence can be attributed to the solid solution strength, which is a result of the high configurational entropy of the HEAs<sup>17</sup>.

### Microstructural characterization

SEM/EDS analysis in Fig. 3 depicts the detailed microstructural examination of AlCrFeNiCu and AlCrFeNiCo-based HEAs. Microstructural characterization plays an important role in understanding HEA properties

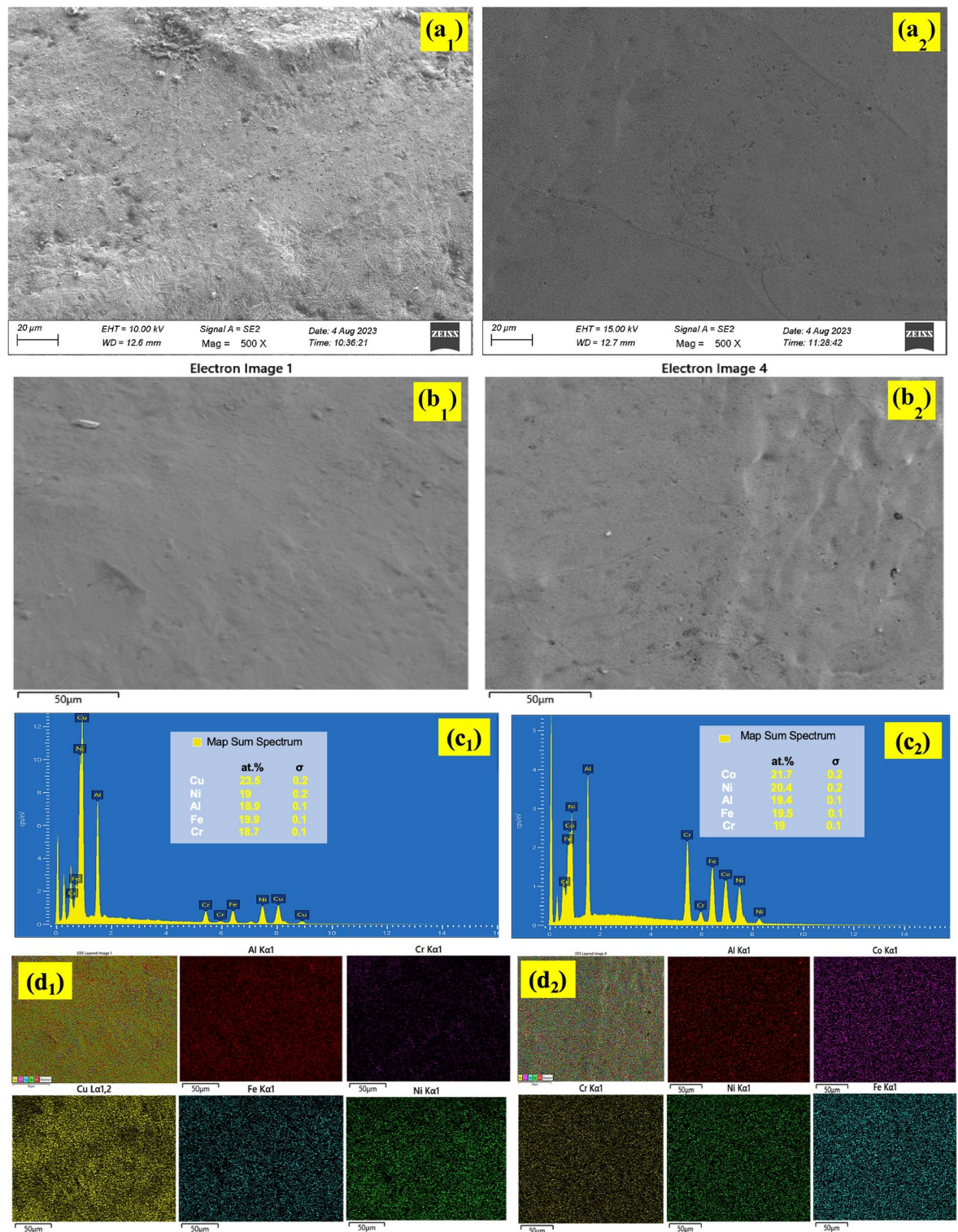


**Fig. 3.** SEM/EDS Analysis (1) AlCrFeNiCu, (2) AlCrFeNiCo: (a) SEM image, (b) EDS Analysis region, (c) Elemental point mapping, (d) Elemental area mapping.

because they exhibit unique properties due to the random distribution of multiple principal elements at near-equiatomic ratios. The micrographs from the SEM of the AlCrFeNiCu and AlCrFeNiCo at 500× magnification are shown in Fig. 3a<sub>1</sub> and a<sub>2</sub>. Surface morphologies of both alloys have appeared to be relatively smooth and fine texture indicates the fine-grained microstructural features. Uniformities in the microstructure might be directly associated with controlled processing conditions prevailing in alloy fabrication, probably to minimize defects like porosity or segregation. From the micrographs, the smoothness and the absence of any phase separation or inclusions suggest that the alloying elements have been well integrated at the microscopic levels. However, on the surface morphology, the texture seems to be a little more for AlCrFeNiCu (a<sub>1</sub>) than AlCrFeNiCo (a<sub>2</sub>); thus, it may suggest differences in the mode of solidification or phase distribution. This could relate to a better-developed microstructure of AlCrFeNiCo and therefore fewer phase boundaries initiate superior mechanical properties.

EDS analysis help to judge the extent of homogeneity of the elemental distribution and the generation of a homogenized fully solid solution phase by establishing a visual of the exact position of each of the elements that are in the alloy system. Figures 3b<sub>1</sub> and 3b<sub>2</sub> offer the spot-by-spot elemental distribution in the alloy matrices. The composition of AlCrFeNiCu (Fig. 3c<sub>1</sub>) exhibits Cu at 23.5 at%, Ni at 19.0 at%, Al at 18.9 at%, Fe at 19.9 at%, and Cr at 18.7 at%. High-entropy alloys have a homogenous solid solution phase due to their equal distribution of elements. The presence of Cu as a significant component would have led to localized phase separation, mainly due to its larger atomic radius and different chemical properties. On the other hand, the EDS result for AlCrFeNiCo (Fig. 3c<sub>2</sub>) indicates that the composition of this is primarily composed of Co (21.7 at%), Ni (20.4 at%), Al (19.4 at%), Fe (19.5 at%), and Cr (19.0 at%). The replacement of Cu with Co has several implications for the alloy's mechanical and chemical properties. Co forms a solid solution strengthening and thus hardening the alloy while enhancing its thermal stability and the corrosion resistance of alloys. This effect is truly significant in the case of oxidation and high-temperature environments.

Elemental mappings in Figs. 3d<sub>1</sub> and d<sub>2</sub> show that EDS results are consistent with these results. Colour-coded maps provide a spatial distribution of elements across the alloy surfaces. At a microscopic scale, elemental maps for Al, Cr, Fe, Ni, and Cu of AlCrFeNiCu (d<sub>1</sub>) reveals a uniform distribution, indicative of a well-mixed alloy. A slight nonuniform distribution of Cu, often with locally higher intensities in the top-left part of the map, may indicate some sort of localized segregation. Precipitates or softer phases formed in the alloy may weaken it by forming a rich Cu region, lowering its hardness. Elemental maps for AlCrFeNiCo (d<sub>2</sub>) show a uniform distribution of all the elements without meaningful signs of segregation. This is important in an elemental alloy because it ensures that the mechanical properties are homogeneous throughout the solid solution phase. Notable in the Co distribution is its distribution-evenness, which indicates that the substitution of Cu for Co has increased the alloy's homogeneity and improved hardness.

### EBSD analysis

The results of the EBSD analysis shown in Fig. 4 shed important light on the grain structure and crystallographic orientation of the synthesized HEAs. The grain's crystallographic orientation within the prepared HEA specimens is depicted by the Inverse Pole Figure (IPF) map, which is shown in Fig. 4a. This map aids in the visualization of the orientation and distribution of grains, revealing details about the preferred orientations and texture of the material. The phase mapping of the HEAs is given in Fig. 4b. The BCC phase is present in the majority of the map for the AlCrFeNiCu alloy, whereas the FCC phase is present in smaller areas. These phases show a complicated microstructure because of its grain boundary orientation. On the other hand, only the BCC phase is present in the AlCrFeNiCo alloy; no other phases are visible. Typically, when alloying atoms with larger differences in atomic size are used, they tend to prefer the body-centred cubic (BCC) structure. This preference is due to the reduction of lattice distortion and the resulting stabilization, which is one of the main advantages of high-entropy alloys (HEA)<sup>18,19</sup>. That implies a simpler and more homogeneous microstructure than the alloy that contained Cu. The distinction in grain size between the HEAs that include Cu and those that contain Co is verified by Fig. 5a. The copper-containing alloy exhibits a larger average grain size of 220.75 μm, while the cobalt-containing alloy has a smaller average grain size of 116.6 μm. The alloy composition or processing parameters may be to blame for the Cu-containing alloy's higher grain size. The variations in grain size affect the alloys' mechanical characteristics. Given its smaller grain size, the Co-containing alloy is probably going to be harder than the Cu-containing alloy. This conclusion is consistent with the microhardness data, indicating that the Co-containing alloy does exhibit increased hardness. The increased Gibbs free energy in the Co-containing alloy can be explained by its smaller particle size<sup>20</sup>. This implies that larger energy fluctuations in the Co-containing alloy cause smaller grains to develop during the solidification and subsequent processing steps.

According to the analysis of Fig. 6a, the fraction of lower angle grain boundaries (LAGB) with misorientation angles ranging from 1 to 15° (represented in red) is significantly lower for both samples than the fraction of higher angle grain boundaries (HAGB) with misorientation angles greater than 15° (shown in blue). This observation implies that in the Cu-containing and Co-containing alloys, there is a higher prevalence of grain boundary misorientations. The grains in the Co-containing alloy exhibit a mono-dispersive nature with equiaxed shapes, as evidenced by Fig. 6a<sub>2</sub>. In contrast, the Cu-containing alloy displays poly-dispersive grains with irregular shapes. This difference in grain morphology between the two alloys may stem from variations in their composition or processing conditions. Additionally, a little soft Face-Centred Cubic (FCC) structure is seen at the grain boundaries in the Cu-containing alloy. This characteristic leads to a decrease in hardness in contrast to the Co-containing alloy, which is devoid of this kind of structure. Lower hardness may result from the soft FCC phase present at the grain boundaries, which can also have an impact on the alloy containing Cu's overall mechanical characteristics. A little rise in the Kernel Average Misorientation (KAM) value is shown in Fig. 7a. This rise is associated with increased residual stress and decreased grain boundary cracking. According to these findings, the nano-grained structures depicted in Fig. 8a, characterized by uniform size and homogeneous dispersion, exhibit

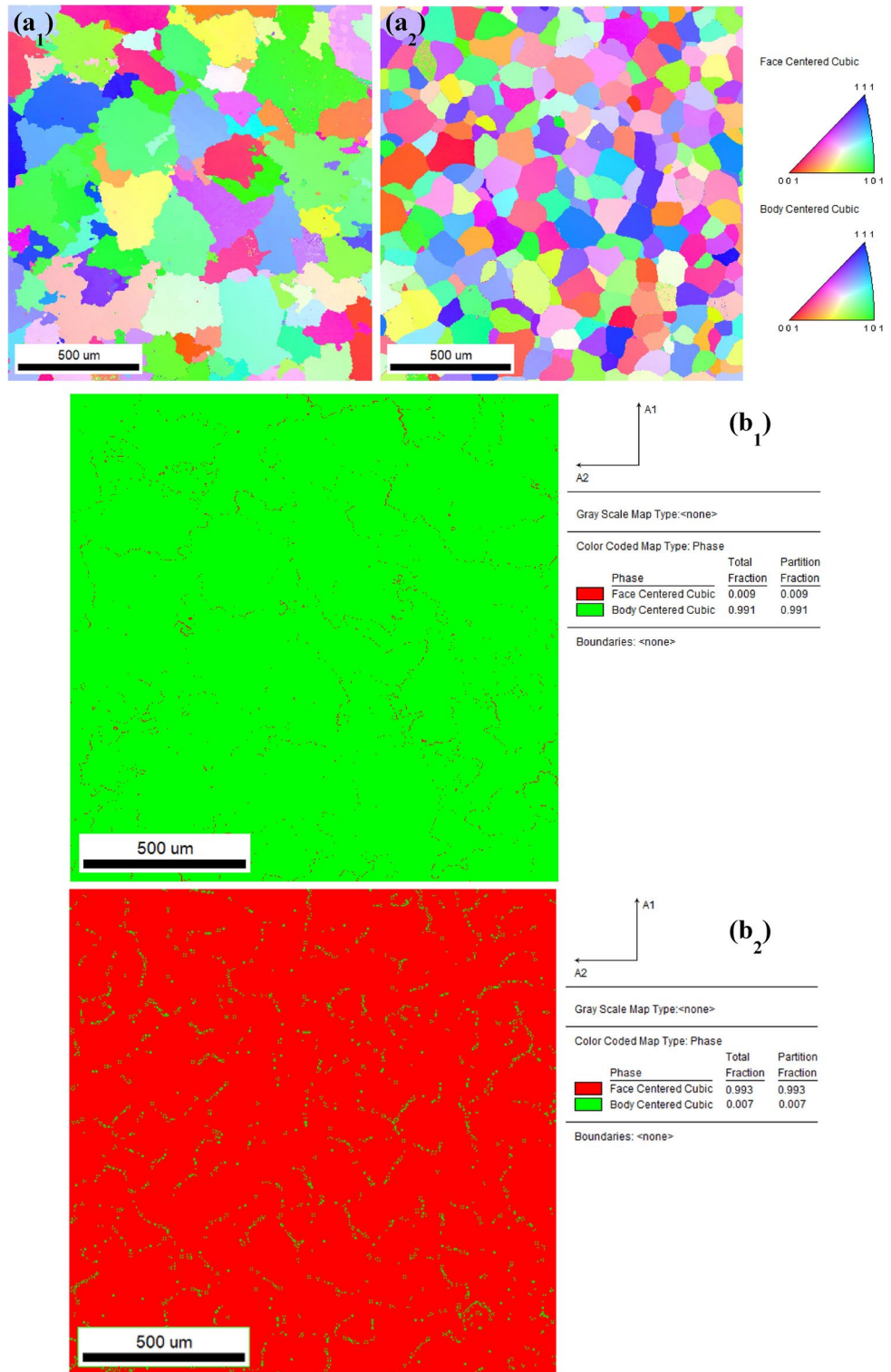


**Fig. 4.** EBSD analysis  $(1)$  AlCrFeNiCu,  $(2)$  AlCrFeNiCo: **(a)** IPF image, **(b)** Phase Mapping.

higher Schmid factors. These increased Schmid factors lead to denser structures with enhanced mechanical strength and wear resistance<sup>21</sup>.

### Microhardness analysis

The average microhardness values for the as-cast samples of AlCrFeNiCu and AlCrFeNiCo alloys were  $415 \pm 10.5$  HV and  $474.4 \pm 8$  HV, respectively, according to the microhardness measurements. These results point to a significant difference in the two alloys' microhardness, with the Co-containing alloy showing greater hardness

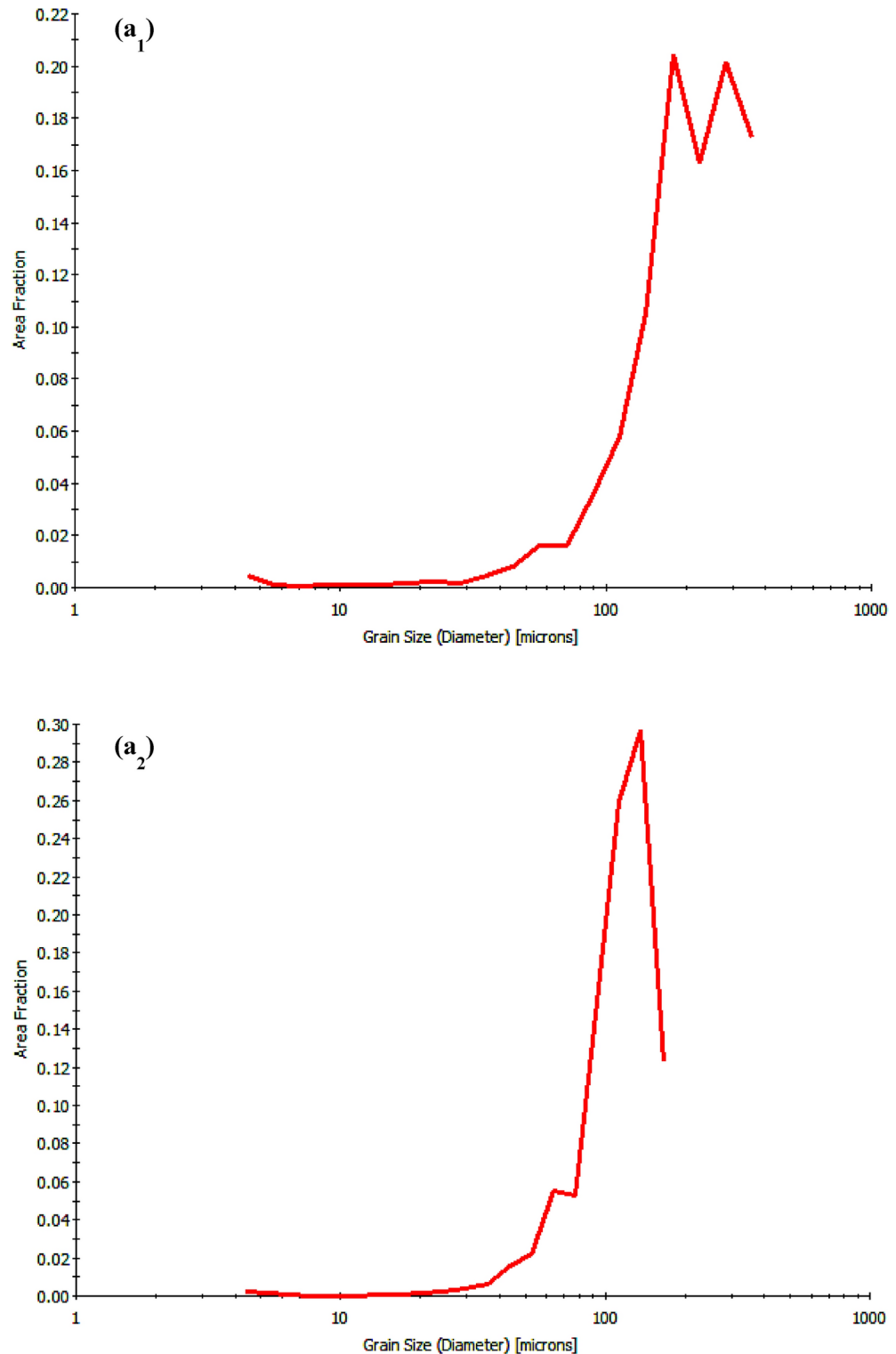


**Fig. 5.** EBSD analysis (<sub>1</sub>) AlCrFeNiCu, (<sub>2</sub>) AlCrFeNiCo: (a) Grain size distribution.

than the Cu-containing alloy. It is noteworthy that for the AlCrFeNiCu<sup>22</sup> and AlCrFeNiCo<sup>23,24</sup> alloys, the quoted hardness values hold true at various loads. This consistency highlights the durability of the observed hardness values by demonstrating the accuracy and repeatability of the hardness measurements.

The X-ray diffraction (XRD) data confirms the increase in hardness in the Co-containing alloy is due to the BCC phase formation. The AlCrFeNiCo alloy demonstrates enhanced mechanical properties, particularly hardness, as a result of the dominant BCC phase present in the alloy, in contrast to the AlCrFeNiCu alloy. This

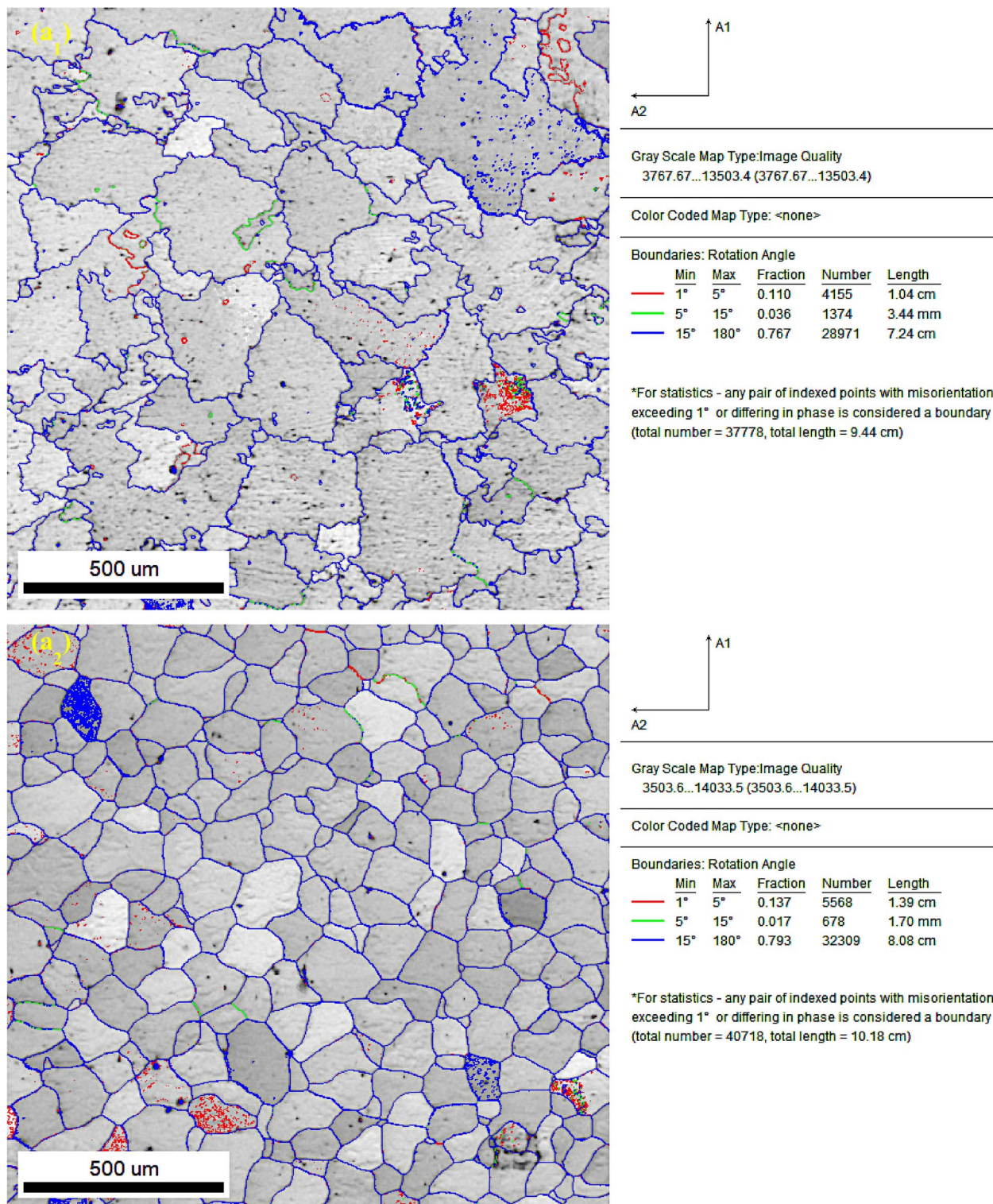


**Fig. 6.** EBSD analysis ( $\zeta_1$ ) AlCrFeNiCu, ( $\zeta_2$ ) AlCrFeNiCo: (a) Grain boundaries.

aligns with the general trend observed in HEAs, where the incorporation of certain alloying elements (Co), promotes BCC phase formation, which exhibits superior hardness compared to other crystal structures.

### Wear analysis

The conditions mentioned in Table 2 have been selected based on the specifications of the experimental setup. The wear rate demonstrates statistical significance for a specific set of wear characteristics in processed samples that have been analyzed using ANOVA. The layout and outcomes of the wear experimentation are shown in

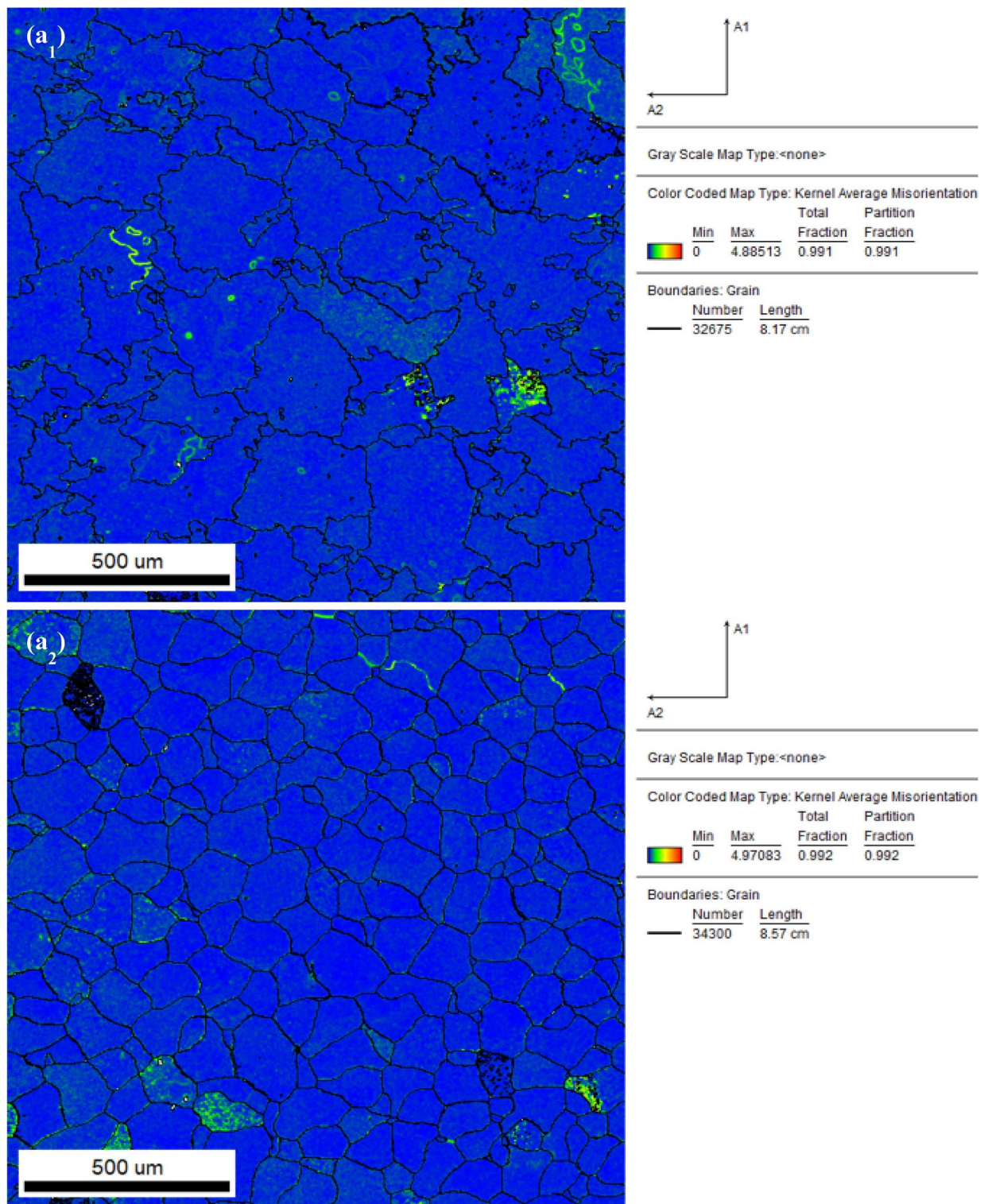


**Fig. 7.** EBSD analysis (<sub>1</sub>) AlCrFeNiCu, (<sub>2</sub>) AlCrFeNiCo: (a) KAM mapping.

Table 3 for both HEAs. The experimental results are assessed using regression models to create a mathematical model for the ideal wear response<sup>25</sup>.

Table 4 gives the response table for the mean wear rate. According to the table, load (N) has the greatest impact on wear rate, followed by sliding velocity and distance. The wear rate variation is proportionate to the stress on the pin surface, according to the application of Archard's law.

More wear loss results from the higher applied load because of constant contact between the surfaces. As a result, increasing the load to create the maximum contact pressure between the material of the counter disc and

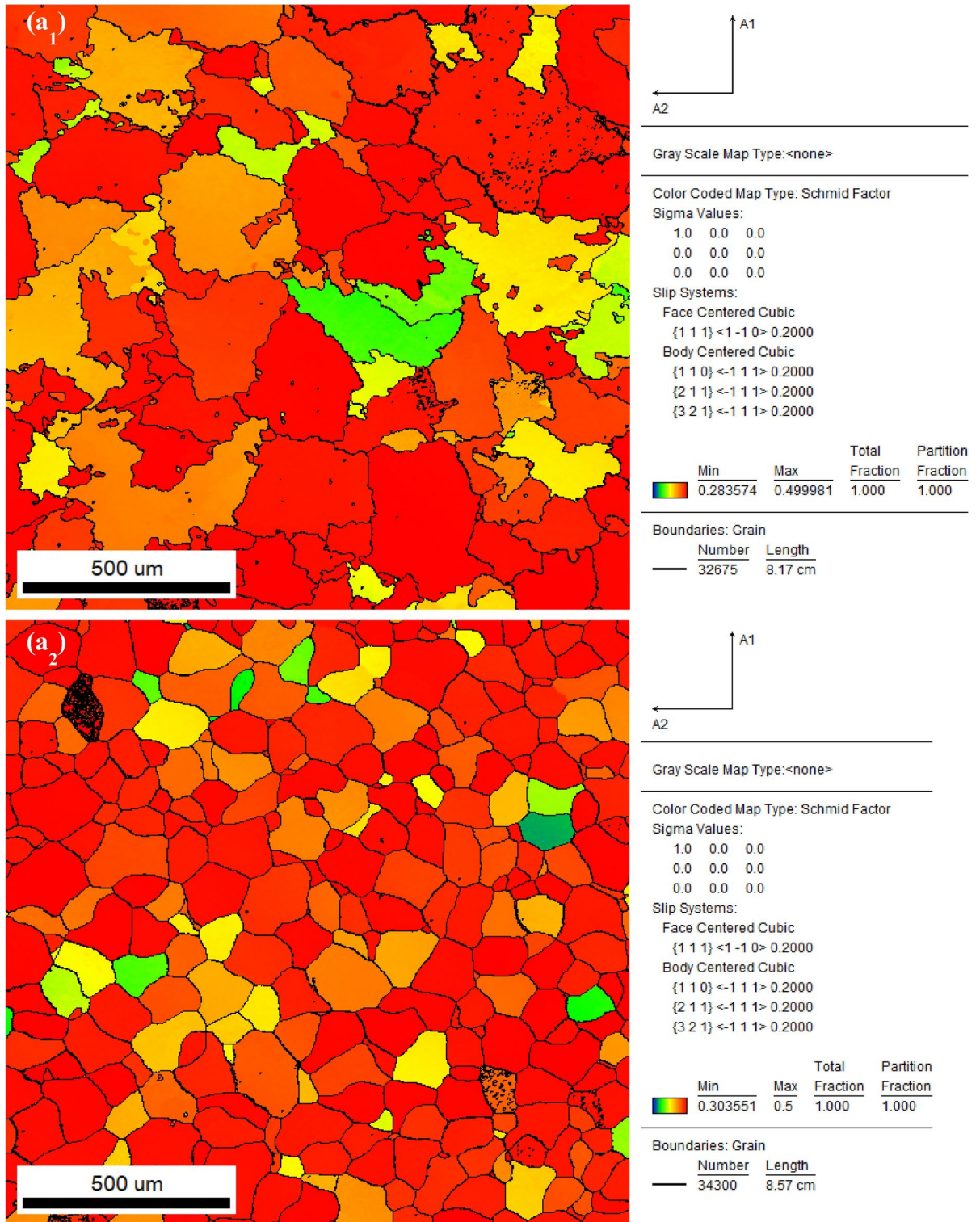


**Fig. 8.** EBSD analysis (<sub>1</sub>) AlCrFeNiCu, (<sub>2</sub>) AlCrFeNiCo: **(a)** The Schmid factor.

the test specimen surface raises the temperature at the interface, increasing the wear rate<sup>26</sup>. Table 4 shows that the load at a level of 10 N, sliding velocity at a level of 3.5 ms<sup>-1</sup>, and sliding distance at a level of 500 m are the optimal levels of parameter combinations that yield the lowest wear rate.

Figure 9a<sub>1</sub>, a<sub>2</sub> indicates that the mean response significantly increases as the load applied increases from 10 to 40 N. This suggests that lower loads may have a positive effect on the wear rate. This indicates that the wear rate increases with greater sliding distances, suggesting a strong positive effect of sliding distance on the response. The plot shows that the mean response rises with higher sliding velocities, particularly between 2.0 and 3.5 m/s.

Load (N)	Sliding distance (m)	Sliding velocity (m/s)	Wear rate (mm <sup>3</sup> /Nm)	
			AlCrFeNiCu alloy	AlCrFeNiCo alloy
10	500	0.5	$6.785 \times 10^{-5}$	$6.05625 \times 10^{-5}$
10	1250	2	$5.321 \times 10^{-5}$	$5.0615 \times 10^{-5}$
10	2000	3.5	$1.00156 \times 10^{-4}$	$9.705 \times 10^{-5}$
25	500	2	$6.248 \times 10^{-5}$	$5.718 \times 10^{-5}$
25	1250	3.5	$7.5472 \times 10^{-5}$	$6.6696 \times 10^{-5}$
25	2000	0.5	$1.3256 \times 10^{-4}$	$1.23835 \times 10^{-4}$
40	500	3.5	$1.0095 \times 10^{-4}$	$8.17 \times 10^{-5}$
40	1250	0.5	$1.8156 \times 10^{-4}$	$1.609 \times 10^{-4}$
40	2000	2	$2.36675 \times 10^{-5}$	$2.1695 \times 10^{-4}$

**Table 3.** Experimental response for the wear parameter analysis of HEAs.

Alloy	Level	Load (N)	Sliding distance (m)	Sliding velocity (m/s)
AlCrFeNiCu	1	$7.4 \times 10^{-5}$ *	$7.7 \times 10^{-5}$ *	$1.27 \times 10^{-4}$
	2	$9.0 \times 10^{-5}$	$1.03 \times 10^{-4}$	$1.17 \times 10^{-4}$
	3	$1.73 \times 10^{-4}$	$1.56 \times 10^{-4}$	$9.2 \times 10^{-5}$ *
	Delta	$9.9 \times 10^{-5}$	$7.9 \times 10^{-5}$	$3.5 \times 10^{-5}$
	Rank	1	2	3
AlCrFeNiCo	1	$6.9 \times 10^{-5}$ *	$6.6 \times 10^{-5}$ *	$1.15 \times 10^{-4}$
	2	$8.3 \times 10^{-5}$	$9.3 \times 10^{-5}$	$1.08 \times 10^{-4}$
	3	$1.53 \times 10^{-4}$	$1.46 \times 10^{-4}$	$8.2 \times 10^{-5}$ *
	Delta	$8.4 \times 10^{-5}$	$7.9 \times 10^{-5}$	$3.3 \times 10^{-5}$
	Rank	1	2	3

**Table 4.** Response table for mean wear rate of HEAs. \*Optimal level.

This suggests that higher sliding velocities positively influence the response variable, though the increase is more gradual compared to the sliding distance. The overall trends and interpretations remain consistent, indicating how the factors influence the response variable for both alloys.

According to the interaction plot (Fig. 9b<sub>1</sub>, 9b<sub>2</sub>), a parallel line denotes no parameter interaction, whereas a nonparallel line denotes a substantial parameter interaction on wear rate. The relationship between load and sliding velocity is shown in Fig. 9 to be significant at lower load 10 N and inconsequential at higher loads. It is evident from the plots of Fig. 9, that the main effects and interaction plots of AlCrFeNiCo and AlCrFeNiCu alloy have the same optimal level statistically. Though it shows a difference from the metallurgical point of view, statistically it is the same from the wear rate point of view.

The higher the applied load more the wear rate for all the sliding velocity. The fact that the applied load and sliding distance did not significantly interact in Fig. 9 suggests that the lines of interaction were nearly parallel except for the load 10 N. Figure 9 illustrates that at higher sliding velocity levels, an increase in sliding distance increases the wear rate. As a result, with a high sliding distance and low sliding velocity, the wear rate was decreased. Nonetheless, when the sliding distance increased, the wear rate of the high load and high sliding velocity combination increased. At any sliding distance, the composite's minimum wear rate can be found at a moderate or least sliding velocity.

A correlation between the input process parameters was established using the regression equation. The association between the control parameters considered to achieve the least wear rate is provided by regression Eqs. (1 and 2) for Cu and Co-based HEAs, respectively. The wear rate on any specimens can be statistically found using the below given regression equations.

$$\begin{aligned}
 \text{Wear Rate (mm}^3/\text{(Nm))} = & 1.12 \times 10^{-4} - 3.9 \times 10^{-5} \text{Load (N)}_{10} \\
 & - 2.2 \times 10^{-5} \text{Load (N)}_{25} + 6.1 \times 10^{-5} \text{Load (N)}_{40} \\
 & - 3.5 \times 10^{-5} \text{Sliding Distance (m)}_{500} - 9.0 \times 10^{-6} \text{Sliding Distance (m)}_{1250} \\
 & + 4.4 \times 10^{-5} \text{Sliding Distance (m)}_{2000} + 1.5 \times 10^{-5} \text{Sliding Velocity (m/s)}_{0.5} \\
 & + 5.0 \times 10^{-6} \text{Sliding Velocity (m/s)}_{2.0} \\
 & - 2.0 \times 10^{-5} \text{Sliding Velocity (m/s)}_{3.5}
 \end{aligned} \quad (1)$$

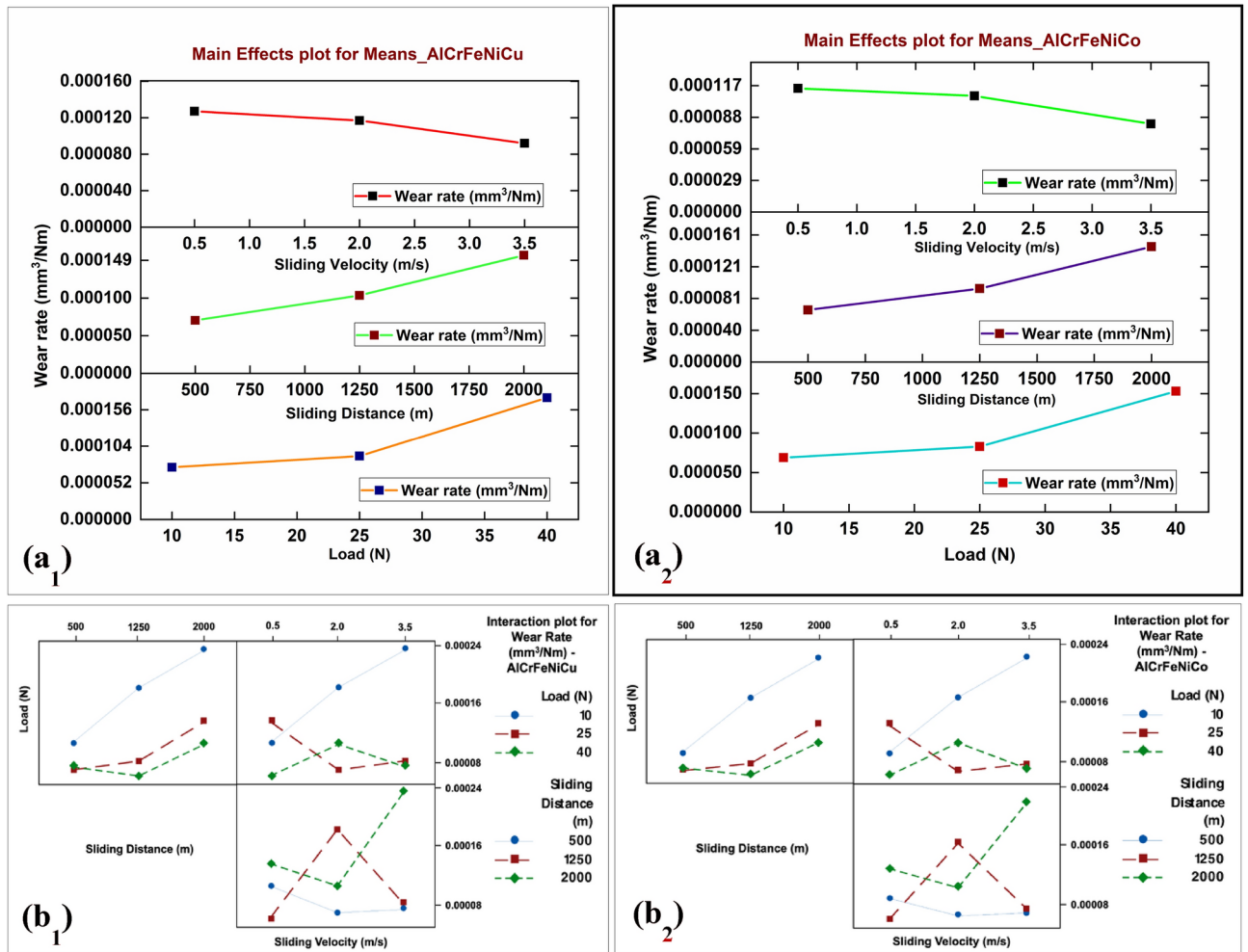


**Fig. 9.** Wear analysis (1) AlCrFeNiCu, (2) AlCrFeNiCo: (a) Main effect plots for Means, (b) Wear rate interaction plots.

$$\begin{aligned}
 \text{Wear Rate (mm}^3\text{/Nm)} = & 1.02 \times 10^{-4} - 3.2 \times 10^{-5} \text{Load (N)}_{10} \\
 & - 1.9 \times 10^{-5} \text{Load (N)}_{25} + 5.1 \times 10^{-5} \text{Load (N)}_{40} \\
 & - 3.5 \times 10^{-5} \text{Sliding Distance (m)}_{500} - 9.0 \times 10^{-6} \text{Sliding Distance (m)}_{1250} \\
 & + 4.4 \times 10^{-5} \text{Sliding Distance (m)}_{2000} + 1.3 \times 10^{-5} \text{Sliding Velocity (m/s)}_{0.5} \\
 & + 7.0 \times 10^{-6} \text{Sliding Velocity (m/s)}_{2.0} - 2.0 \times 10^{-5} \text{Sliding Velocity (m/s)}_{3.5}
 \end{aligned} \quad (2)$$

The ANOVA findings for the wear rate of two different HEAs are displayed in Table 5. It is confirmed that load is the most significant parameter, with a contribution of 56.21% and 48.31% for AlCrFeNiCo and AlCrFeNiCu alloys, respectively. It is followed by sliding distance with a percentage contribution for AlCrFeNiCo and AlCrFeNiCu alloys of 32.41% and 39.03%, respectively. The sliding velocity is the least significant parameter, with 6.51% and 7.33% in both HEAs. The R-sq values of 95.12% and 94.68% of the wear rate of AlCrFeNiCo and AlCrFeNiCu alloys are found and are given in Table 6. From the R-sq values, it is evident that the parameters chosen for the present experimentation are correct and can be utilized in any specimen following the same experimental procedures for the conduct of wear analysis. It is understood that the model can predict the response with high accuracy for both HEAs as given in the table.

Essentially, a higher R-squared tells you that the independent variable(s) in your model account for a larger share of the changes observed in the dependent variable. This translates to a more precise model for predicting the dependent variable based on the independent variables. AlCrFeNiCo shows increased microhardness, whereas AlCrFeNiCu demonstrates superior wear resistance attributed to the presence of the FCC phase. It is capable of absorbing and dissipating greater amounts of energy during wear, which lessens the intensity of wear mechanisms like delamination and adhesion. Co plays a crucial role in refining the grain of the processed HEA. The AlCrFeNiCo alloy exhibited a smaller average grain size, which increases in microhardness by 14.21% than AlCrFeNiCu HEA. These observations highlight the effectiveness of Co in enhancing the strength of the alloy and complement current research showing that Co promotes grain refinement and improves mechanical

Sources	DF	Adj SS	Adj MS	F-value	P value	% contribution
AlCrFeNiCu alloy						
Load (N)	2	$1.701 \times 10^{-8}$	$8.50 \times 10^{-9}$	11.52	0.080	56.21%
Sliding distance (m)	2	$9.81 \times 10^{-9}$	$4.90 \times 10^{-9}$	6.64	0.131	32.41%
Sliding velocity (m/s)	2	$1.97 \times 10^{-9}$	$9.8 \times 10^{-10}$	1.33	0.428	6.51%
Error	2	$1.48 \times 10^{-9}$	$7.4 \times 10^{-10}$			4.89%
Total	8	$3.026 \times 10^{-8}$				100%
AlCrFeNiCo alloy						
Load (N)	2	$1.218 \times 10^{-8}$	$6.09 \times 10^{-9}$	9.07	0.099	48.31%
Sliding distance (m)	2	$9.84 \times 10^{-9}$	$4.92 \times 10^{-9}$	7.33	0.120	39.03%
Sliding velocity (m/s)	2	$1.85 \times 10^{-9}$	$9.3 \times 10^{-10}$	1.38	0.420	7.33%
Error	2	$1.34 \times 10^{-9}$	$6.7 \times 10^{-10}$			5.31%
Total	8	$2.521 \times 10^{-8}$				100%

**Table 5.** Analysis of variance for HEAs.

Alloy	S	R-sq	R-sq (adj)
AlCrFeNiCu	$2.72 \times 10^{-5}$	95.12%	80.49%
AlCrFeNiCo	$2.59 \times 10^{-5}$	94.68%	78.70%

**Table 6.** Mean summary of analysis of variance for HEAs.

properties. The BCC structure in Co-HEA exhibits significant hardness; however, this increased hardness comes at the cost of brittleness, resulting in elevated wear rates under specific conditions.

### Worn surface morphology

The study classifies the intricate worn surface morphology of AlCrFeNi-based High Entropy Alloys (HEAs) that contain Cu and Co components by describing numerous surface characteristics and wear mechanisms. The worn surface morphology provided validation for the mechanisms linked to wear behaviour. It is possible to comprehend wear-related features, such as oxide layers, grooves, cracks, delamination, pits, etc., by looking at the surface morphology.

Figure 10a<sub>1</sub>, a<sub>2</sub> displays the worn surface morphology of AlCrFeNiCu and AlCrFeNiCo alloys with the highest wear rate conditions. Worn surfaces frequently exhibit deep grooves. Deeper grooves are the outcome of harder asperities or third-body particles infiltrating the material surface. The sliding velocity and applied load affect the depth and width of these grooves; larger loads and velocities cause more noticeable grooving because of the increased stress and temperature at the contact locations<sup>27,28</sup>. Surface layers peel off when subsurface fissures spread parallel to the surface, resulting in visible delamination. Increased thermal and mechanical pressures weaken the surface layers and the underlying material bonding, making this wear process more common at greater loads and sliding velocities. Delamination can significantly accelerate both the wear rate and material loss. Adhesive wear is another method of material transfer between touching surfaces. As a result, layers of sticky material build on the surface that has worn down. Asperities from one surface cling to the other and spread over the area of contact, creating these layers. The material's characteristics and the operating environment influence how adhesive layers form and remain stable. The intricate relationships among the many alloying elements in HEAs can help or impede the development of solid adhesive layers<sup>29</sup>. The worn surface has small, localized depressions that suggest pitting. The separation of material fragments, often as a consequence of corrosion or subsurface fatigue processes, causes the formation of these pits. Cu and Co additions can change the alloy's resistance to corrosion, which in turn can change the pitting behaviour. Increased stress concentration and the promotion of pit initiation are two ways that higher loads and sliding velocities can worsen pitting<sup>30,31</sup>.

Figure 10b<sub>1</sub>, b<sub>2</sub> illustrates the worn surface shape of the alloys AlCrFeNiCu and AlCrFeNiCo under minimum wear rate conditions. The wear mechanism in these HEAs depends on the worn surface oxide layers. The frictional heat during sliding raises the temperature at the interface, which may encourage the oxidation of the alloying components. The presence of elements such as Cr and Al aids in the development of protective oxide layers. By preventing direct metal contact and lowering the wear rate, these oxide layers may serve as a barrier. However, high loads and speeds have the potential to wear away the oxide layers, exposing the underlying material to more abrasion. Hard asperities or particles that are less deeply buried in the surface are typically abrasive, creating shallow grooves on worn surfaces<sup>32,33</sup>. Additionally, microcracks and fissures on the worn surfaces, point to the fatigue wear process. These cracks start because of cyclic loading and recurrent stress concentrations at specific surface locations. Larger cracks, which result from the convergence of microcracks, can eventually remove material. Because each element has unique mechanical properties that offer varying degrees of resistance to fracture formation, the presence of elements such as Co and Cu can affect the behaviour of crack propagation.

The experimental findings demonstrate the connection between the wear mechanisms and the process parameters (weight, sliding velocity, and sliding distance). Elevated loads and sliding velocities typically intensify

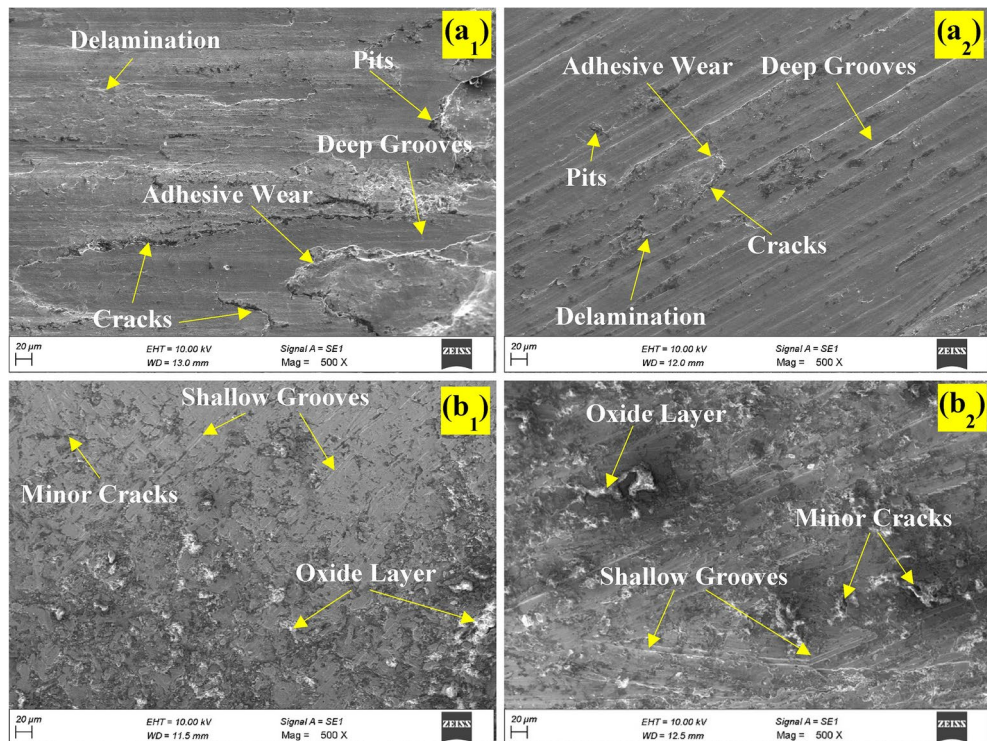


**Fig. 10.** Worn Surface Morphology analysis of HEA alloys (<sub>1</sub>) AlCrFeNiCu, (<sub>2</sub>) AlCrFeNiCo: (a) Highest wear rate, (b) Lowest wear rate.

surface damage mechanisms such as grooving, delamination, adhesive wear, and pitting, leading to an increased wear rate. Conversely, by lessening the severity of these mechanisms, moderate to high sliding velocities (3.5 m/s) and high loads (10 N) can minimize wear rate. The regression equations derived from the experimental data provide a mathematical explanation of these interactions and aid in process parameter optimization for the lowest wear rates of the Cu and Co-based HEAs.

## Conclusions

This work examined the microstructure, phases formed, and microhardness of two different vacuum arc melted HEAs, AlCrFeNiCu and AlCrFeNiCo. The following is a summary of the present research:

- *Phase formation* X-ray Diffraction (XRD) investigation confirmed that the Cu-containing alloy displayed a combined BCC and FCC structure, while both AlCrFeNiCu and AlCrFeNiCo HEAs displayed a combination of crystal structures. Conversely, the Co-containing alloy exhibited a mainly BCC crystal structure.
- *Grain size and microhardness* The Cu-containing HEA exhibited a greater average grain size compared to the Co-containing HEA. The difference in grain size led to a notable rise in microhardness, with the Co-based HEA alloy exhibiting a microhardness increase of 14.21% in comparison to the Cu-based alloy.
- *Grain morphology* The alloy containing cobalt displayed equiaxed grain morphology, which means that the grains had a consistent size and shape. The mean grain size of this alloy was determined to be 116.6 μm, suggesting a comparatively finer grain structure in comparison to the alloy containing copper.
- The experimental results demonstrate that the wear rate of both AlCrFeNiCo and AlCrFeNiCu HEAs is mostly influenced by the load. Higher loads lead to increased wear rates. The optimal conditions for minimising wear rate were seen with a load of 10 N, a sliding velocity of 3.5 m/s, and a sliding distance of 500 m. These findings suggest that controlling the applied load is crucial for reducing wear. The study shows that this holds for both high-entropy alloys (HEAs), however, the HEA including copper has slightly superior wear resistance compared to the HEA containing cobalt.
- An analysis of the worn surface morphology of AlCrFeNi-based HEAs containing Cu and Co components shows that higher loads (40 N) and sliding velocities (0.5 m/s) worsen wear mechanisms such as grooving, delamination, adhesive wear, and pitting, leading to an increased wear rate. On the other hand, lower loads (10 N) and higher velocities (3.5 m/s) encourage the development of protective oxide layers, which decrease the wear rate.

## Data availability

The datasets used and/or analysed during the current study available from the corresponding author on reasonable request.

Received: 9 August 2024; Accepted: 14 October 2024

Published online: 09 November 2024

## References

1. Praveen, S. & Kim, H. S. High-entropy alloys: Potential candidates for high-temperature applications—An overview. *Adv. Eng. Mater.* **20**, 1700645 (2018).
2. Kumar, D. Recent advances in tribology of high entropy alloys: A critical review. *Prog. Mater. Sci.* **136**, 101106 (2023).
3. Nahmany, M., Hooper, Z., Stern, A., Geanta, V. & Voiculescu, I. AlxCrFeCoNi high-entropy alloys: Surface modification by electron beam bead-on-plate melting. *Metall. Microstruct. Anal.* **5**, 229–240 (2016).
4. Senkov, O. N., Wilks, G. B., Miracle, D. B., Chuang, C. P. & Liaw, P. K. Refractory high-entropy alloys. *Intermetallics* **18**, 1758–1765 (2010).
5. Kong, L., Cheng, B., Wan, D. & Xue, Y. A review on BCC-structured high-entropy alloys for hydrogen storage. *Front. Mater.* **10**, 1135864 (2023).
6. Sathishkumar, M. et al. Possibilities, performance and challenges of nitinol alloy fabricated by directed energy deposition and powder bed fusion for biomedical implants. *J. Manuf. Process.* **102**, 885–909 (2023).
7. Vignesh, M. et al. Development of biomedical implants through additive manufacturing: A review. *J. Mater. Eng. Perform.* **30**, 4735–4744 (2021).
8. Serban, B.-A. et al. Non-aqueous electrodeposition and characterization of AlCrCuFeNi high entropy alloy thin films. *Materials* **15**, 6007 (2022).
9. Noble, N., Radhika, N., Sathishkumar, M. & Saleh, B. Characterisation and property evaluation of high entropy alloy coating on 316L steel via thermal spray synthesis. *Tribol. Int.* **185**, 108525 (2023).
10. Luo, S. et al. Selective laser melting of an equiatomic AlCrCuFeNi high-entropy alloy: Processability, non-equilibrium microstructure and mechanical behavior. *J. Alloys Compd.* **771**, 387–397 (2019).
11. Bi, P., Hashimoto, N., Hayashi, S., Oka, H. & Isobe, S. Effect of Al on oxidation behavior of AlxCrCuFeNi<sub>2</sub> (x = 0.2, 0.4, 0.6) high entropy alloys. *Corros Sci* **208**, 110697 (2022).
12. Haghdad, N. et al. The scratch behaviour of AlXCoCrFeNi (x = 0.3 and 1.0) high entropy alloys. *Wear* **428–429**, 293–301 (2019).
13. Wu, J.-M. et al. Adhesive wear behavior of AlXCoCrCuFeNi high-entropy alloys as a function of aluminum content. *Wear* **261**, 513–519 (2006).
14. Chen, J. et al. Mechanical and tribological characterisation of AlCoCuFeNi HEA reinforced magnesium composites prepared via spark plasma sintering. *Proc. Inst. Mech. Eng. Part L J. Mater. Des. Appl.* **236**, 2074–2084 (2022).
15. Wang, X. et al. Microstructure and mechanical property of novel nanoparticles strengthened AlCrCuFeNi dual-phase high entropy alloy. *Mater. Today Commun.* **32**, 104155 (2022).
16. Ma, X., Xin, D., Ye, J., Guo, J. & Li, H. Comparative study of the microstructure evolution of dual-phase Al–Co–Cr–Fe–Ni high-entropy alloy prepared by direct laser deposition and vacuum arc melting. *Mater. Lett.* **326**, 132951 (2022).
17. Hamdi, H., Abedi, H. R. & Zhang, Y. A review study on thermal stability of high entropy alloys: Normal/abnormal resistance of grain growth. *J. Alloys Compd.* **960**, 170826 (2023).
18. Kube, S. A. et al. Phase selection motifs in high entropy alloys revealed through combinatorial methods: Large atomic size difference favors BCC over FCC. *Acta Mater.* **166**, 677–686 (2019).
19. Kumar, G. R. et al. Metallographic characterization of laser peened Ti6Al4V subjected to hydrogen charging. *J. Mater. Eng. Perform.* <https://doi.org/10.1007/s11665-023-08099-7> (2023).
20. Locci, A. M. On the experimental assessment of thermodynamic stability of nanostructured solid solutions. *Mod. Concepts Mater. Sci.* **2**, 000537 (2019).
21. Sakai, T., Belyakov, A., Kaibyshev, R., Miura, H. & Jonas, J. J. Dynamic and post-dynamic recrystallization under hot, cold and severe plastic deformation conditions. *Prog. Mater. Sci.* **60**, 130–207 (2014).
22. Liu, Y. et al. Tribological properties of AlCrCuFeNi<sub>2</sub> high-entropy alloy in different conditions. *Metall. Mater. Trans. A Phys. Metall. Mater. Sci.* **47**, 3312–3321 (2016).
23. Wang, M. et al. Fabrication of hydrophobic AlCoCrFeNi high-entropy alloy and superior corrosion resistance to NTO aqueous solution. *J. Alloys Compd.* **915**, 165394 (2022).
24. Radhika, N., Noble, N. & Adediran, A. A. Electrochemical and hot corrosion behaviour of annealed AlCoCrFeNi HEA coating over steel. *Sci. Rep.* **14**, 5652 (2024).
25. Baradeswaran, A., Elayaperumal, A. & Issac, R. F. A statistical analysis of optimization of wear behaviour of Al–Al<sub>2</sub>O<sub>3</sub> composites using taguchi technique. *Proc. Eng.* **64**, 973–982 (2013).
26. Veeravalli, R. R., Nallu, R. & Mohiuddin, S. M. M. Mechanical and tribological properties of AA7075–TiC metal matrix composites under heat treated (T6) and cast conditions. *J. Mater. Res. Technol.* **5**(4), 377–383 (2016).
27. Joseph, J. et al. The sliding wear behaviour of CoCrFeMnNi and AlXCoCrFeNi high entropy alloys at elevated temperatures. *Wear* **428–429**, 32–44 (2019).
28. Jin, B., Zhang, N., Yu, H., Hao, D. & Ma, Y. AlXCoCrFeNiSi high entropy alloy coatings with high microhardness and improved wear resistance. *Surf. Coat. Technol.* **402**, 126328 (2020).
29. Verma, A. et al. High temperature wear in CoCrFeNiCu high entropy alloys: The role of Cu. *Scr. Mater.* **161**, 28–31 (2019).
30. Xu, Z., Li, D. Y. & Chen, D. L. Effect of Ti on the wear behavior of AlCoCrFeNi high-entropy alloy during unidirectional and bidirectional sliding wear processes. *Wear* **476**, 203650 (2021).
31. Radhika, N., Krishna, S. A., Basak, A. K. & Adediran, A. A. Microstructure and tribological behaviour of CoCrCuFeTi high entropy alloy reinforced SS304 through friction stir processing. *Sci. Rep.* **14**, 3662 (2024).
32. Liu, S. S., Zhao, G. L., Wang, X. H. & Zhou, C. J. Design and characterization of AlNbMoTaCu high entropy alloys laser cladding coatings. *Surf. Coat. Technol.* **447**, 128832 (2022).
33. Zhang, M. et al. Microstructure and elevated temperature wear behavior of laser-cladded AlCrFeMnNi high-entropy alloy coating. *Opt. Laser Technol.* **149**, 107845 (2022).

## Author contributions

M.V., M.S., M.S., and S.M.M., wrote the main manuscript text and V.M., M.S., N.R., K.D, and S.R.M. prepared Figs. 1, 2, 3, 4, 5, 6, 7, 8, 9 and 10. All authors reviewed the manuscript.

## Declarations

## Competing interests

The authors declare no competing interests.

### Additional information

**Correspondence** and requests for materials should be addressed to M.S.

**Reprints and permissions information** is available at [www.nature.com/reprints](http://www.nature.com/reprints).

**Publisher's note** Springer Nature remains neutral with regard to jurisdictional claims in published maps and institutional affiliations.

**Open Access** This article is licensed under a Creative Commons Attribution-NonCommercial-NoDerivatives 4.0 International License, which permits any non-commercial use, sharing, distribution and reproduction in any medium or format, as long as you give appropriate credit to the original author(s) and the source, provide a link to the Creative Commons licence, and indicate if you modified the licensed material. You do not have permission under this licence to share adapted material derived from this article or parts of it. The images or other third party material in this article are included in the article's Creative Commons licence, unless indicated otherwise in a credit line to the material. If material is not included in the article's Creative Commons licence and your intended use is not permitted by statutory regulation or exceeds the permitted use, you will need to obtain permission directly from the copyright holder. To view a copy of this licence, visit <http://creativecommons.org/licenses/by-nc-nd/4.0/>.

© The Author(s) 2024